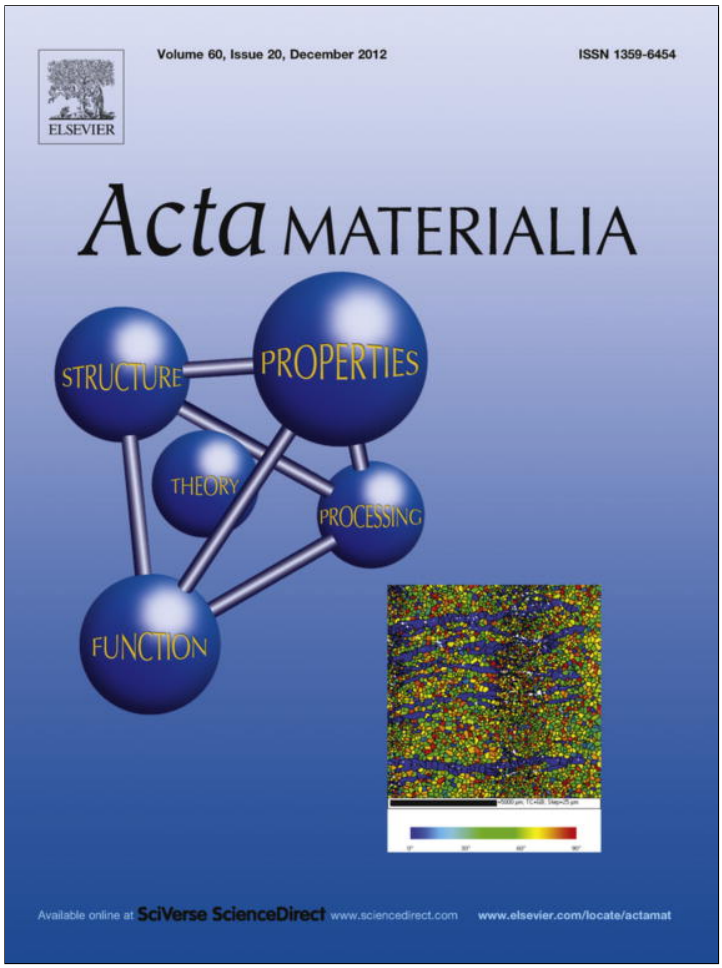

Available online at www.sciencedirect.com

SciVerse ScienceDirect

Acta Materialia 60 (2012) 7160–7168

Acta MATERIALIA

www.elsevier.com/locate/actamat

Novel ultrafine Fe(C) precipitates strengthen transformation-induced-plasticity steel

G.K. Tirumalasetty [a,b,*], C.M. Fang [b], Q. Xu [b], J. Jansen [b], J. Sietsma [c], M.A. van Huis [d,b], H.W. Zandbergen [b]

[a] Materials innovation institute (M2i), Mekelweg 2, 2628 CD Delft, The Netherlands
[b] Kavli Institute of Nanoscience, Delft University of Technology, Lorentzweg 1, 2628 CJ Delft, The Netherlands
[c] Department of Materials Science and Engineering, Delft University of Technology, Mekelweg 2, 2628 CD Delft, The Netherlands
[d] Soft Condensed Matter, Debye Institute for Nanomaterials Science, Utrecht University, Princetonplein 5, 3584 CC Utrecht, The Netherlands

Received 15 July 2012; received in revised form 23 August 2012; accepted 10 September 2012
Available online 5 October 2012

Abstract

A transmission electron microscopy study was conducted on nanoprecipitates formed in Ti microalloyed transformation-induced-plasticity-assisted steels, revealing the presence of Ti(N), Ti_2CS and a novel type of ultra-fine Fe(C) precipitate. The matrix/precipitate orientation relationships, sizes and shapes were investigated in detail. The ultrafine, disc-shaped Fe(C) precipitates have sizes of 2–5 nm and possess a hexagonal close packed crystal structure with lattice parameters $a = 5.73 \pm 0.05$ Å, $c = 12.06 \pm 0.05$ Å. They are in a well-defined Pitsch–Schrader orientation relationship with the basal plane of the precipitate parallel to the [1 1 0] habit plane of the surrounding body-centred-cubic ferritic matrix. Detailed analysis of precipitate distribution, orientation relationship, lattice mismatch and inter-particle spacing suggests that these ultrafine precipitates contribute considerably to the strengthening of these steels.

Keywords: TRIP assisted steel; Iron carbides; Precipitation; Transmission electron microscopy

1. Introduction

Ever-increasing demands of automotive industries for steels possessing higher strengths and enhanced ductility have led to the development of transformation-induced-plasticity (TRIP)-assisted steels. The improved mechanical properties in these materials are attributed to composite deformation of microstructural environments consisting of phases like ferrite, austenite, bainite and martensite [1]. During deformation, the austenite grains in these steels undergo both rotations and transformations to martensite whereby the onset of necking is postponed, leading to improved ductility in these steels through the TRIP effect [2]. While the tensile strength of TRIP steels is typically between 600 and 800 MPa, TRIP steels with higher tensile strengths, in excess of 800 MPa, are becoming increasingly important for automotive applications considering the high demands on weight reduction and safety requirements [3].

This level of strength can be achieved by ferritic grain size refinement in combination with dispersion strengthening. In general, microalloying is adopted for this purpose by using elements such as Nb, V or Ti [4]. It is well known that transition metals like Nb, V or Ti have the tendency to interact with interstitial elements such as C and N, forming precipitates [5–7]. Among Nb, V and Ti, Ti is thermodynamically the first element to precipitate during solidification. This element effectively bonds with nitrogen and produces Ti(N) at higher temperatures [5] and it can also result in the formation of several complex Ti-containing compounds in ferrite [8]. In order to understand the

* Corresponding author at: Kavli Institute of Nanoscience, Delft University of Technology, Lorentzweg 1, 2628 CJ Delft, The Netherlands. Tel.: +31 15 2781536; fax: +31 15 2786600.
E-mail address: g.k.tirumalasetty@tudelft.nl (G.K. Tirumalasetty).

1359-6454/$36.00
http://dx.doi.org/10.1016/j.actamat.2012.09.025

precipitation sequence and to determine the possible contribution to effective strengthening of these steels, a detailed characterization of these nanoscale compounds is essential.

Therefore, the aim of the present work is to carry out a thorough investigation of precipitates formed in Ti microalloyed TRIP steel using transmission electron microscopy (TEM) and to analyse their structural properties in relation to precipitation hardening. As will be shown in detail below, we found various types of precipitates: Ti(N), Ti_2CS and Fe(C), whereby the latter one to our best knowledge has not been reported before. Below we first discuss the experimental procedure in Section 2, and continue with optical microscopy and TEM results in Section 3. In Sections 3.2–3.5, a detailed analysis is given of the size, shape and crystal structures of the precipitates, and the orientation relationships with the surrounding ferritic matrix. In Section 3.6 strengthening mechanisms are discussed and the Orowan–Ashby model is used to make a quantitative estimate of the additional contribution of the ultrafine Fe(C) precipitates to the strengthening.

2. Experimental procedure

The chemical composition of the investigated Al-alloyed TRIP-assisted steel with Ti micro-additions is listed in Table 1. These steels are produced on an industrial hot dip galvanizing line using a conventional intercritical annealing cycle followed by cooling to ~400–460 °C, isothermal holding it at this temperature and finally cooling it to room temperature. The rolled TRIP steel sheets were cut into slices along the normal direction (ND)–transverse direction (TD) plane and the microstructures of the specimens were studied by optical microscopy (OM). The specimen preparation for optical examination involved a stepped etching procedure as suggested by De et al. [9]. The samples for transmission electron microscopy (TEM) were mechanically pre-thinned along the ND–TD plane using SiC paper. Thin foils were prepared by twin-jet electropolishing using a solution of 100 ml perchloric acid and 300 ml butanol in 500 ml methanol at 20 V and a temperature of −20 °C. The conventional TEM analysis was carried out using a Philips CM30T and a Philips CM200 both operating at 200 kV. Both selected area diffraction (SAD) and nano-diffraction (ND) were employed to study the nano-sized precipitates in this steel. High-resolution transmission electron microscopy (HRTEM) and energy dispersive X-ray spectroscopy (EDX) of the samples were carried out in a FEI Tecnai F20ST/STEM microscope with an EDAX analysis system operating at a voltage of 200 kV.

3. Results and discussion

It has long been recognized that the addition of microalloying additions can significantly alter the ferritic grain size as well as the final microstructure. Therefore, we first discuss briefly the general microstructure.

3.1. Light microscopic analysis of microstructures

The microstructure of investigated steels is shown in Fig. 1, in which the large brown areas represent ferrite, and the greyish blue areas represent bainite. Retained austenite is etched white, while the martensite grains present off-white tone in the optical micrograph [9]. The fractions of retained austenite, ferrite martensite and bainite in Fig. 1 were quantified using Image Analyser. The retained austenite constitutes 9.5%, and martensite, bainite and ferrite constitute 1.2%, 19.9% and 62%, respectively, while the remaining 7.4% of the area fraction is due to the grain boundaries. It can be seen from Fig. 1 that the average ferrite grain size of this steel is about 8 μm, which is large in comparison with Nb alloyed TRIP steel having an average ferritic grain size of 5 μm [6]. Furthermore, the fractions of austenite are considerably higher than Nb microalloyed TRIP steel [6].

3.2. TEM analysis

Detailed TEM analysis was performed to characterize the various precipitates found in this steel. Fig. 2a shows a ferrite grain in a (0 0 1) orientation as identified by electron diffraction in Fig. 2b. The ferrite grain contains precipitates with different sizes and morphologies: (a) precipitates with cubic morphology and a size range of 70–120 nm, (b) faceted precipitates with a size range of 40–70 nm and (c) spherical precipitates with a size range of 20–100 nm as shown in the schematic representation in Fig. 2c. In addition (d), ultrafine disc-shaped precipitates with a size range of 2–5 nm are also seen in Fig. 2a. These four (cubic, faceted, spherical and disc) types of precipitates (Ti(N), Ti(N), Ti_2CS and ultrafine Fe(C)) are subsequently discussed below.

3.3. Analysis of precipitates containing Ti and N

As observed in Fig. 2a there are precipitates with cubic and faceted morphologies in the ferritic matrix. They are distributed throughout the steel and possess wide size dispersions. EDX analysis was carried out to identify the chemical composition. From the elemental analysis shown

Table 1
Chemical composition (wt.%) of Al alloyed TRIP-assisted steel with Ti micro-addition.

C	Mn	Si	Al	Cr	Ti	V	P	S	N
0.187	1.620	0.350	0.917	0.020	0.009	0.003	0.087	0.003	<0.0001

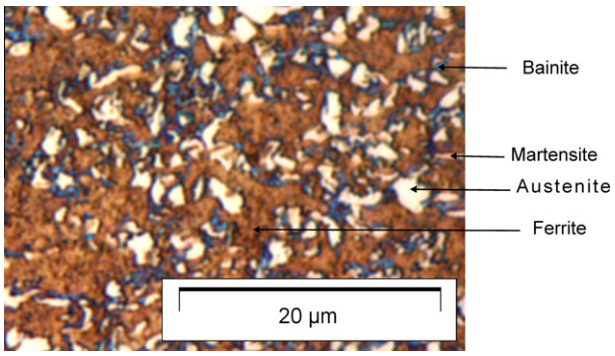

Fig. 1. Optical microstructure of Al alloyed TRIP-assisted steel with Ti micro-addition.

Table 2
EDX analysis of the TiN precipitates with cubic and faceted morphologies.

Element	wt.%	wt.% error	at.%
A. Cubic Ti(N) precipitate			
N	29.94	2.03	59.92
Ti	58.98	1.49	34.51
Fe	11.07	0.73	5.56
Total	100.00	–	100.0
B. Faceted Ti(N) precipitate			
N	4.92	1.62	16.61
Ti	20.63	0.59	20.36
Fe	74.44	1.19	63.02
Total	100.00	–	100.0

in Table 2 it is evident that both the cubic and faceted precipitates contain high concentrations of Ti and N. With the EDX analysis, minor contributions from Al, Si, Mn and Fe also appear in these precipitates since the EDX signal in TEM comes not only from the precipitate but also from the matrix phase surrounding the precipitate, as a large part of the sample is hit by stray electrons. In addition, in general there is a contribution of the matrix material on top of and beneath the precipitate. The cubic precipitate shown in Fig. 3a is at the edge of the electropolished area and has very little matrix on top of or beneath it, and thus the spurious Fe signal is relatively low in comparison to that of the faceted precipitates. Interestingly, the cubic shaped precipitates showed a higher N content than the faceted precipitates. In order to assess the crystal structure and possible orientation relationships with the matrix, nano-diffraction was performed. Fig. 3b and d shows diffraction patterns of cubic shaped precipitates and faceted shaped Ti(N) precipitates in (1 0 0) orientations. Both these precipitates were identified to have the face-centred cubic (fcc) crystal structure. The lattice parameter of cubic precipitates was $a = 4.5 \pm 0.05$ Å while in the case of faceted precipitates the observed lattice parameter was $a = 4.3 \pm 0.05$ Å. The measured lattice spacings of faceted precipitates are very close to that of the well-known TiN crystal structure [10], whereas the cubic shaped precipitates showed a slightly larger lattice parameter. These differences may be caused by different N contents [11]. The Ti(N) precipitates were found in random orientations and had no preferred orientation relationship with the surrounding ferrite matrix.

It is well known that precipitation of TiN occurs in two temperature regimes: during solidification of the steel, and in supersaturated austenite after solidification. Coarse TiN precipitates are formed at liquid iron temperatures of ~1540 °C during solidification [5]. In solidified steel, during δ-γ (austenite) transformation (around 1400 °C), the coarse TiN precipitates undergo enhanced dissolution, leading to Ti enrichment in δ-γ solid solution. At temperatures between 1400 and 1200 °C, precipitation of smaller TiN and Ti_2CS precipitates takes place in supersaturated austenite [5]. Since annealing of steels takes place at ~900–950 °C and given that both TiN and Ti_2CS have higher dissolution temperatures, they are expected to pin the grain boundaries, thereby limiting the recrystallization and grain growth process during hot rolling, leading to refinement of the final ferritic grain size [12].

3.4. Analysis of precipitates containing Ti, C and S

Apart from the Ti(N) precipitates there are also spherical particles which are observed within the ferritic matrix as observed in Fig. 4. EDX analysis in Table 3 shows that these precipitates have much higher concentrations of Ti and S than the surrounding ferrite matrix. Ti and S concentrations of 6.93 and 1.59 at.% respectively, were found in the precipitates, while these elements could not be detected in the matrix. Analysis of the d-spacings of

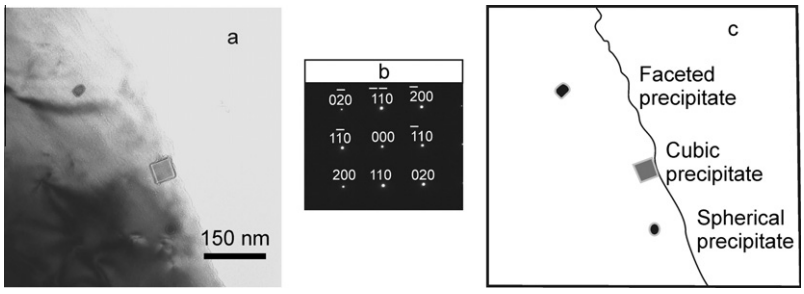

Fig. 2. (a) Bright-field TEM image of a ferrite grain in TRIP-assisted steel showing precipitates with different morphologies. (b) Electron diffraction pattern of ferrite in a (0 0 1) orientation. (c) Schematic representation of the TEM image in (a) with different morphologies of the precipitates indicated.

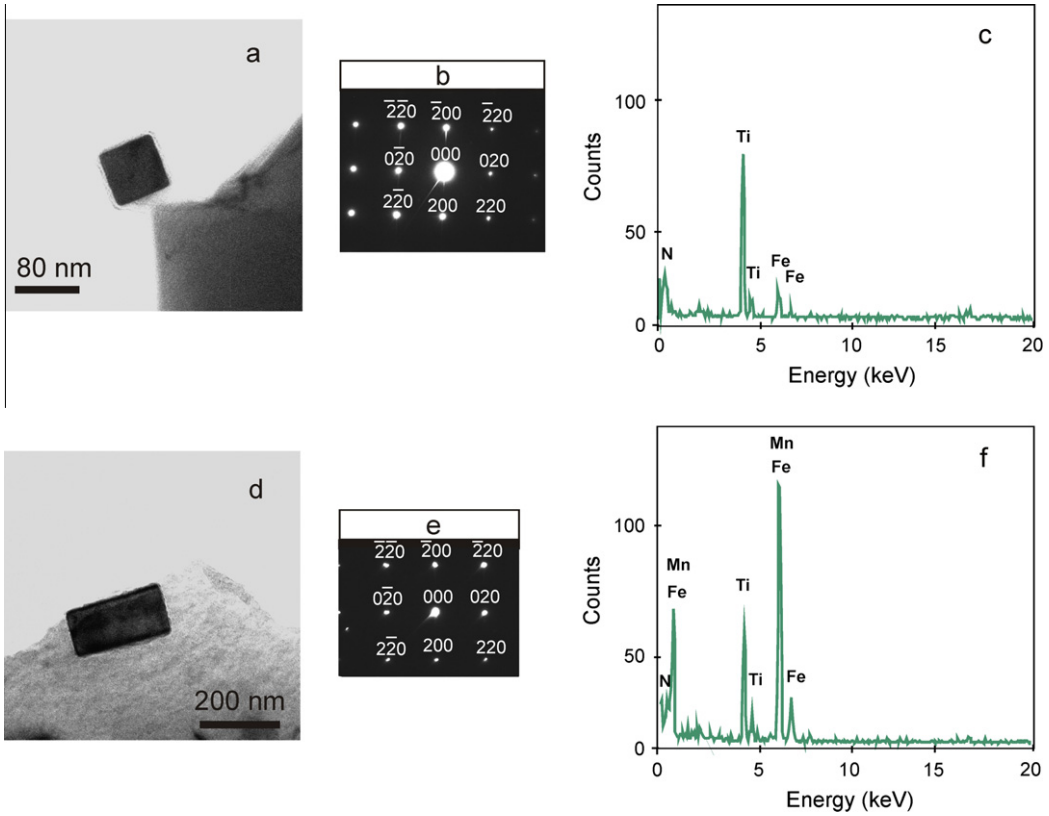

Fig. 3. Ti(N) precipitates in Al alloyed TRIP-assisted steel. (a, d) Bright field TEM images of cubic and faceted Ti(N) precipitates and their (b, e) corresponding diffraction patterns in (0 0 1) orientation. (c, f) Corresponding EDX elemental analysis.

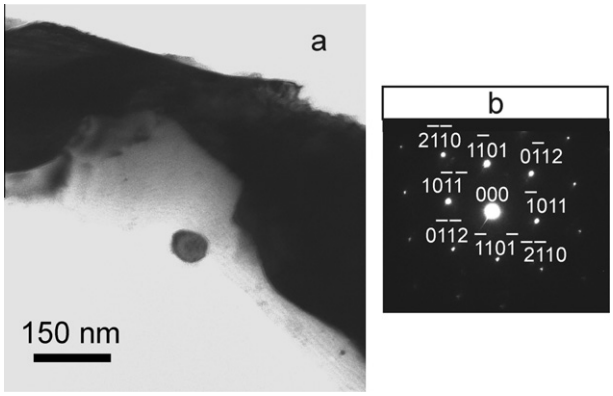

Fig. 4. Ti(C,S) precipitate in Al alloyed TRIP-assisted steel: (a) bright field TEM image showing spherical shaped Ti(C,S) precipitate and its (b) corresponding diffraction pattern in $(0\,1\,\bar{1}\,1)$ orientation.

Table 3
EDX analysis of the Ti_2CS precipitate and the ferrite matrix next to the precipitate.

Element	wt.%	wt.% error	at.%
A. Precipitate			
C	20.12	2.2	53.05
S	1.61	0.38	1.59
Ti	10.48	0.69	6.93
Fe	67.79	1.98	38.44
Total	100.00	–	100.0
B. Ferrite matrix			
C	3.35	1.15	13.68
Al	1.41	0.31	2.56
Mn	1.39	0.36	1.24
Fe	93.85	1.21	82.52
Total	100.00	–	100.0

the nano-diffraction patterns showed that they are in good agreement with well-known Ti_2CS phase [13] having a hexagonal close packed (hcp) structure.

3.5. Analysis of precipitates containing Fe and C

It is well established that Ti microalloying can result in precipitation of stable TiC precipitates having a cube-on-cube Burgers relationship with the surrounding ferrite matrix. Surprisingly, no TiC precipitates were observed in ferrite in the present study. Instead, a new type of ultrafine precipitate was observed having a well-defined orientation relationship with the ferritic matrix. To the best of our knowledge, such precipitates have not been reported before, and a thorough TEM investigation was carried out on these precipitates. The selected area diffraction (SAD) pattern with ferrite in (1 1 0) projection showed Fe(C) precipitates with (0 0 0 1) orientation as seen in Fig. 5a. A dark-field recording using the $[\bar{2}\,\bar{2}\,4\,0]$ reflection in the (0 0 0 1) projection of precipitates is shown in Fig. 5b.

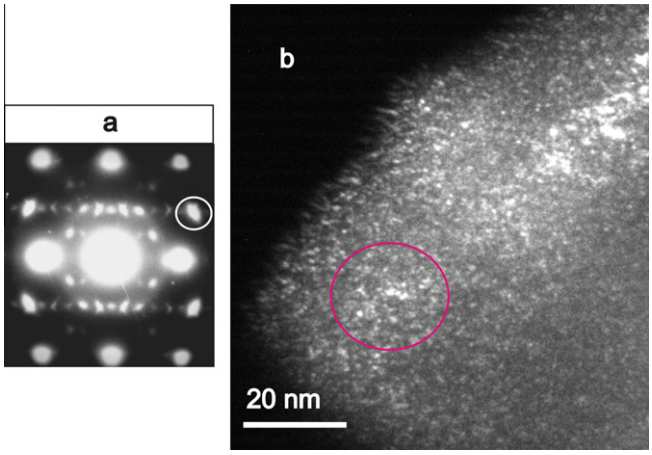

Fig. 5. Fe(C) precipitates in Al alloyed TRIP-assisted steel: (a) SAD pattern where the white circle indicates the [$\bar{2}\,\bar{2}\,4\,0$] reflection of Fe(C). (b) Corresponding dark field image showing the size distribution of Fe(C) precipitates in ferrite using the [$\bar{2}\,\bar{2}\,4\,0$] reflection of Fe(C). The pink circle in the image is used for the estimating the volume fraction of the Fe(C) precipitates. (For interpretation of the references to colour in this figure legend, the reader is referred to the web version of this article.)

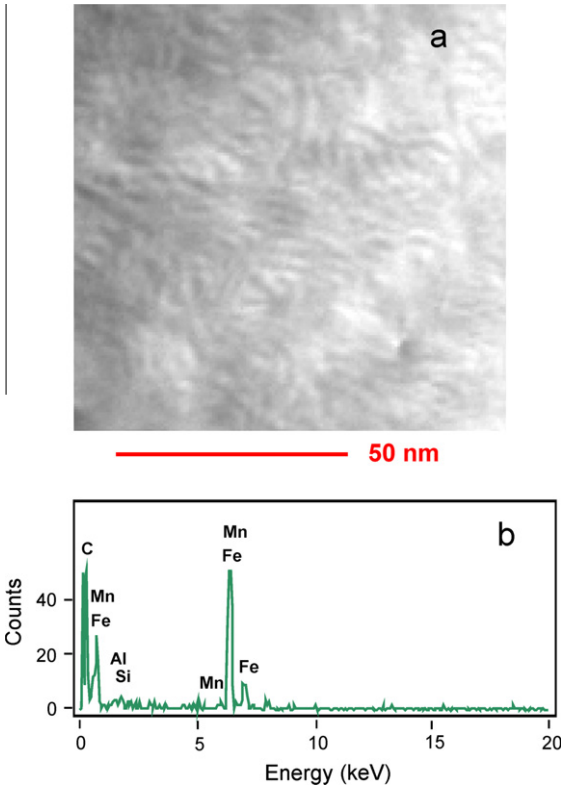

Fig. 6. (a) HAADF STEM image of Fe(C) precipitates in ferrite matrix and (b) the corresponding EDX spot analysis of the precipitate.

Here, all the precipitates that have the same orientation are visible. Furthermore, one can see in Fig. 5b also the size distribution of precipitates to be within a size range of 2–5 nm. The shape of the observed precipitates in Fig. 5b (in particular in the thinner sections at the edge) and the streaking of precipitate reflections seen in the SAD pattern in Fig. 5a, indicate that these precipitates have disc shaped morphologies, which is also confirmed by the STEM image in Fig. 6 that is discussed below.

Since the precipitates are very small, Z-contrast imaging using high angle annular dark field (HAADF) scanning transmission electron microscopy (STEM) was carried out. In the HAADF detector, electrons are collected that are not Bragg scattered and HAADF images show little or no diffraction effects, as their intensity is approximately proportional to Z^2. Fig. 6a shows the STEM-HAADF image of the precipitates in (0 0 0 1) orientation and the neighbouring ferrite matrix aligned along the (1 1 0) orientation. It is evident from this image that there are no significant differences in contrast between the precipitates and the surrounding matrix. Energy dispersive X-ray spectroscopy (EDX) analysis was also carried out on several of these precipitates. The corresponding EDX map in Fig. 6b clearly shows higher concentrations of Fe and C, indicating a $Fe_X(C)_Y$ type of precipitate.

Unit cell reconstruction of precipitates was carried out using tilt series reconstruction from selected area diffraction (SAD) patterns. The precipitate was rotated about the a^* axis and a set of diffraction patterns was recorded. A total of five diffraction patterns were taken along this rotation axis as shown in Fig. 7a–e, allowing a reconstruction of the unit cell. Fig. 7f shows the unit cell reconstruction in reciprocal space. It follows that these precipitates have a hexagonal lattice. The lattice parameters of the precipitate in real space were calculated using the d spacing of α-Fe (ferrite) for calibration. The unit cell parameters of the precipitate phase are $a = 5.73 \pm 0.05$ Å, $b = 5.73 \pm 0.05$ Å, $c = 12.06 \pm 0.05$ Å with $\alpha = 90°$, $\beta = 90°$ and $\gamma = 120°$. Iron carbide with such a unit cell has hitherto not yet been reported (see Table S1 of the Supporting information for a list of all iron carbides [14–22] reported in the literature). Given the size of the a–b plane and that the approximate Fe–Fe bond distances is ~2.5 Å, it is highly likely that the structure is composed of layers stacked along the c-axis whereby there are four Fe atoms in the stacked layer. The length of the c-axis indicates a stacking of six Fe layers. Given the hexagonal symmetry, ABABAB and ABCABC stacking are the most simple and most likely ones. Since the 2 0 0 reflection is strong in all diffraction patterns like those in Fig. 7a–e, the ABCABC stacking can be excluded.

The orientation relationship of these Fe(C) precipitates with respect to the ferritic matrix was investigated. All the diffraction patterns with ferrite in (1 1 0) projection show Fe(C) precipitates with (0 0 0 1) orientation as seen in Fig. 8. Further, the reflections in [0 0 2] of ferrite overlap with [$2\,\bar{4}\,2\,0$] of Fe(C). Thus these Fe(C) precipitates exhibit a definite Pitsch–Schrader (P–S) orientation relationship with the ferrite matrix:

$$(1\,1\,0)\ \alpha\text{-Fe}//(0\,0\,0\,1)\ \text{Fe(C)} \quad (1)$$

$$[0\,0\,1]\ \alpha\text{-Fe}//[1\,\bar{2}\,1\,0]\ \text{Fe(C)} \quad (2)$$

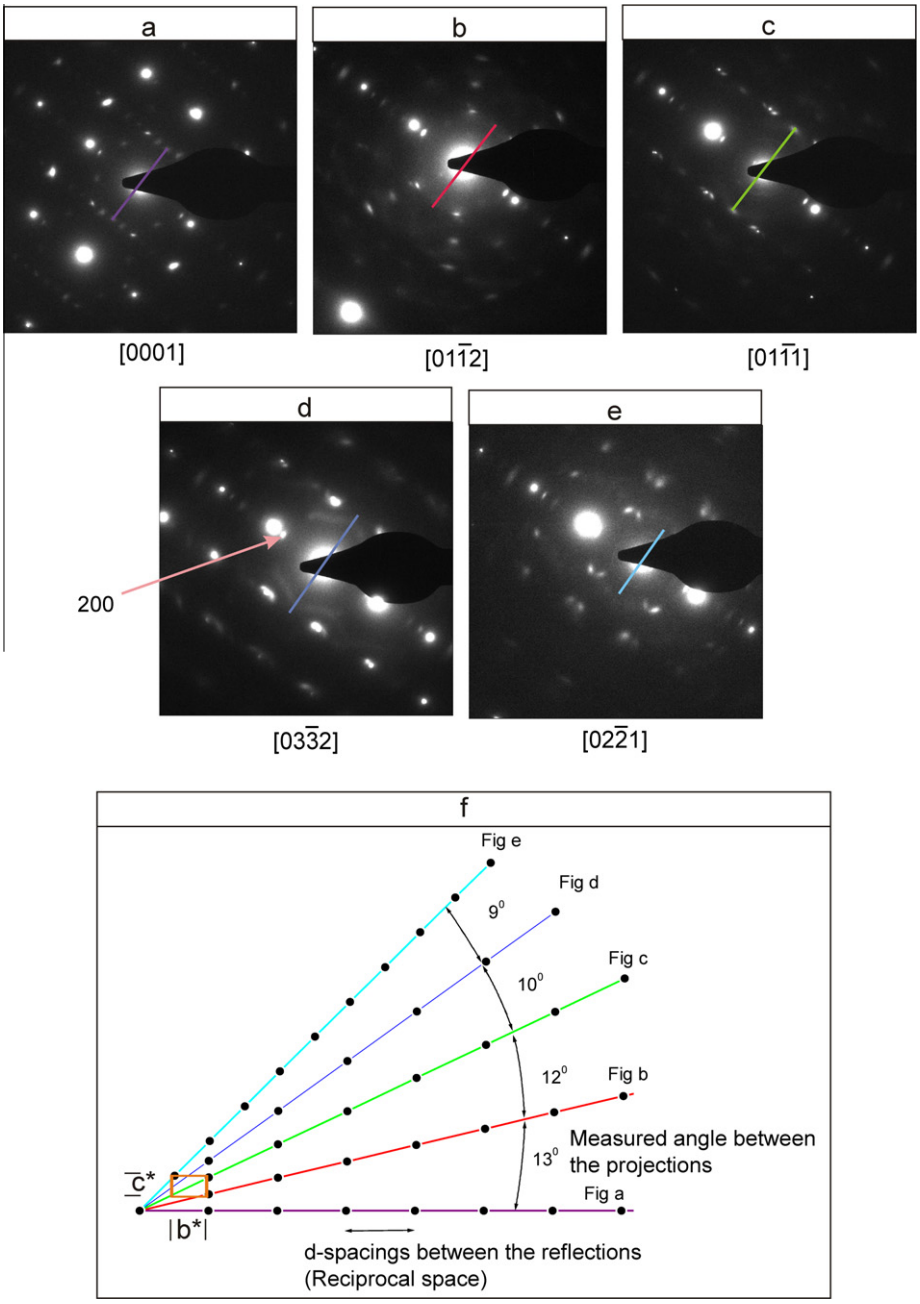

Fig. 7. (a-e) SAD patterns recorded from the Fe(C) precipitate by tilting about a^* axis. The colored lines indicate the d-spacings of the reflections measured perpendicular to the rotation axis. (f) Tilt series reconstruction with the reciprocal lattice points from the series of SAD patterns in (a-e) and with the angles between the projections. The cuboid shows the unit cell of the precipitate in reciprocal space. (d) shows 200 reflection of Fe(C) precipitate. (For interpretation of the references to colour in this figure legend, the reader is referred to the web version of this article.)

Fig. 9 shows a HRTEM image with all Fe(C) precipitates oriented along the (0001) axis when the surrounding α-Fe matrix is oriented along the (110) projection. Thus the observed Fe(C) precipitates within this steel are found to agree with this orientation relationship and hence can be considered as a general feature of Fe(C) /α-Fe precipitate–matrix relationship.

Epsilon carbides were observed previously by Jack [23] with a similar orientation relationship, however the unit cell parameters of the Jack carbides (in particular the *c* parameter) differ substantially from the Fe(C) precipitates found in the present study. Now the question arises as to why such a new Fe(C) precipitate is observed in this particular steel. A comparison of the papers on precipitation of carbides from ferrite shows that new precipitates can be formed as a result of particular heat treatments. For instance, until 1952, it was assumed that cementite (Fe_3C) was the only iron carbide that would form directly from supersaturated ferrite [24]. This viewpoint was supported by kinetic measurements performed by Dijkstra [25] and

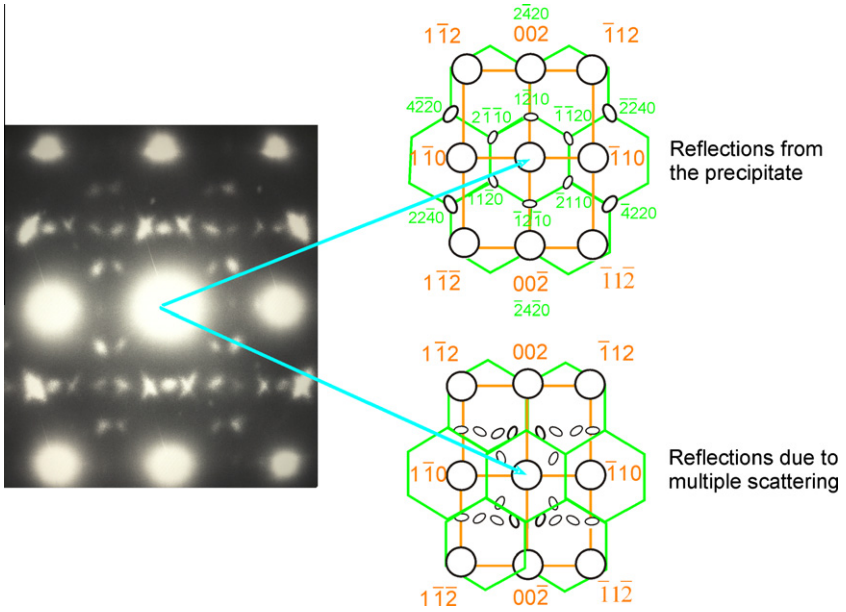

Fig. 8. Fe(C) precipitates in Al alloyed TRIP-assisted steel exhibiting a definite Pitsch Schrader (P-S) orientation relationship with the surrounding ferrite matrix. The Fe(C) precipitate (green) is in a (0001) projection while α-Fe (orange) is in a (110) projection. The additional reflections seen in diffraction pattern are due to the multiple scattering of the electron beam. (For interpretation of the references to colour in this figure legend, the reader is referred to the web version of this article.)

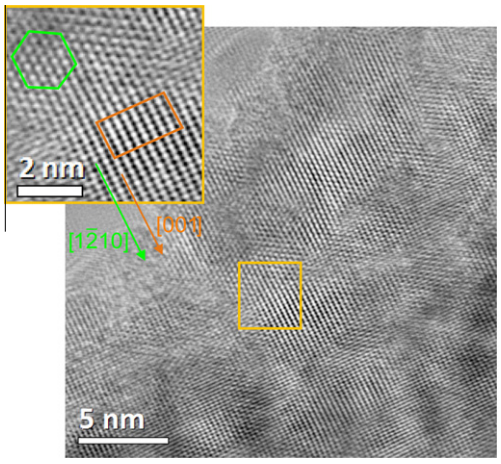

Fig. 9. HRTEM image along the (1 1 0) α-Fe // (0 0 0 1) Fe(C) precipitate. The enlarged inset with a gold border in the figure shows Fe(C) precipitates indicated by green hexagon exhibiting a definite Pitsch–Schrader (P-S) orientation relationship with the ferrite matrix represented by orange rectangle. (For interpretation of the references to colour in this figure legend, the reader is referred to the web version of this article.)

Wert [26] on the precipitation of carbon from quenched iron containing about 0.02 wt.% carbon, which gave no indication of the existence of any metastable phase prior to the formation of cementite. In contrast with these reports, in 1952 Tsou et al. [27] used electron diffraction to reveal the existence of ε-carbide ($Fe_{2.4}C$) in iron containing 0.026 wt.% carbon. Investigations by Bosewell [28] in 1958 confirmed these observations and showed that both carbides could be precipitated from super-saturated solid solution in α-iron. According to Bosewell, cementite precipitates in α-iron during aging above 200 °C, whereas aging at lower temperatures will result in the formation of ε-carbide. Although Bosewell's observations are well established over the years, Leslie et al.'s [29] observations showed that prolonged aging of their steels led to precipitate diffraction patterns that are not compatible with the lattice spacings of well-known ε-carbide and cementite nor of Fe(C) precipitate reported in this paper. From the above literature on iron carbides and our work presented here, it is expected that the occurrence of such new carbides in this steel could be a consequence of temperature and time of the given heat treatment.

3.6. Role of precipitates in strengthening of the steel

An overall objective of the steel industry is to enhance the strength of steel by increasing the strength of the ferrite phase through precipitation hardening. It is therefore important to understand the contribution of the above-mentioned precipitates to effective strengthening of the steels. Table 4 summarizes the size ranges, orientation relationship and crystal structures of precipitates found in this steel. Both Ti(N) and Ti_2CS could be very effective in pinning austenitic grain boundaries [5,18] at elevated temperature during the hot rolling process, as explained above in Section 3.3. On the one hand this could result in reducing the ferritic grain size (grain refinement strengthening), leading to enhancement of yield strength and toughness. On the other hand, the Fe(C) precipitate, which has the highest number density per unit volume and a small or anisotropic lattice mismatch, is expected to act as an obstacle to dislocation movement, raising the overall strength of

Table 4
Summary of precipitates observed in Al alloyed TRIP-assisted steel.

Observed precipitates	Morphology	Size ranges (nm)	Crystal structure	Lattice parameters (Å)	Orientation relationship with ferrite
Ti(N)	Cubic	70–120	fcc	$a = 4.5 \pm 0.05$	No
Ti(N)	Faceted	40–70	fcc	$a = 4.3 \pm 0.05$	No
Ti_2CS	Spherical	20–100	hcp	$a = 3.2 \pm 0.05$ $c = 11.2 \pm 0.05$	No
Fe(C)	Disc	2–5	hcp	$a = 5.73 \pm 0.05$ $c = 12.06 \pm 0.05$	Yes

the steel. There are two well-known mechanisms by which the precipitates can retard the motion of dislocations. The precipitates may be cut by the dislocations, or the precipitates resist cutting so that the dislocations are forced to bypass them through the so-called Orowan mechanism [30]. The mechanism that requires the least energy will be the relevant one for obstructing the dislocation motion. Considering that iron carbides are generally hard and thus resist cutting [31], the Orowan mechanism is most likely the dominant mechanism.

In that case, the contributions of Fe(C) precipitates towards strengthening can be predicted using the Orowan–Ashby model as presented by Gladman [32]:

$$\sigma p = 10.8 \frac{\sqrt{f}}{d} \ln(1630d) \quad (3)$$

where σ_p represents the precipitation strengthening increment in MPa, f is the volume fraction of precipitate, and d is the mean particle diameter in μm.

This model has been shown previously to give very reasonable quantitative estimation for the precipitation strengthening potential of nano-sized carbonitride particles in microalloyed steels [33,34]. From Fig. 5b, it can be seen in that Fe(C) precipitates (in particular at the edge of the specimen) have an average diameter of 3×10^{-3} μm and an approximate thickness of 1×10^{-3} μm. From these numbers, an average volume of the disc-shaped precipitates can be calculated. The volumetric precipitate fraction can then be estimated as follows. Within a circular area having a diameter of 20×10^{-3} μm as indicated in Fig. 5b, ~40 Fe(C) precipitates are counted. Estimating the thickness of the TEM sample at $\sim 200 \times 10^{-3}$ μm, it follows that the volumetric fraction is 45×10^{-4}. This results in a contribution of 383 MPa to strengthening of ferrite according to the above model. Since the steel has 62% area fraction of ferrite according to the image analyser/light microscopic observations as discussed in Section 3.1, the precipitates could result in a potential contribution of 237 MPa to strengthening of this steel.

Additionally, from the experimentally determined lattice parameter of Fe(C) the lattice mismatch was calculated in three mutually perpendicular directions as shown in Table 5. Here the lattice mismatch is calculated with ferrite (α-Fe) as a reference, $\eta = |(d_{Fe(C)} - d_{\alpha\text{-}Fe})/d_{\alpha\text{-}Fe}|$. In two directions, [0 0 1] α-Fe // [1 $\bar{2}$ 1 0] Fe(C) and [1 1 0] α-Fe // [0 0 0 1] Fe(C), there is a good fit with a very small lattice mismatch ($0.0 \pm 1.1\%$). The lattice mismatch along the third direction is 22.3%, suggesting that there is considerable strain in one direction, and little strain in the other two directions, i.e. the precipitates are semi-coherent. A comparison was made with iron carbides that were observed previously in ferrite, i.e. Fe_3C and $Fe_{2.4}C$, with the orientation relationships suggested in the literature [29,35]. From Table 5 it is clear that the observed Fe(C) precipitates are more likely to effectively strengthen steels than the well-known Fe_3C and $Fe_{2.4}C$ phases. Furthermore, it is well known that slip occurs along {1 1 0}, {1 1 2} and {1 2 3} planes in ferrite. Hence, from the above P-S relationship, it is expected that dislocations of (1 1 0) type can effectively be pinned by Fe(C) precipitates resulting in enhanced strengthening of these steels. The above results are undoubtedly of great importance in tailoring the TRIP steels for optimizing mechanical properties. Further, a significant number of ferrite-based steels can strongly benefit from these results.

Table 5
Experimentally obtained lattice parameters and calculated lattice mismatch in between values for α-Fe and Fe(C), Fe_3C, $Fe_{2.4}C$ precipitates.

Lattice parameter	Fe(C) (hcp)	$a = b = 5.73 \pm 0.05$ Å $c = 12.06 \pm 0.05$ Å
	θ-Fe_3C (orthorhombic)	$a = 5.10$ Å $b = 6.77$ Å $c = 4.54$ Å
	ε-$Fe_{2.4}C$ (hcp)	$a = b = 4.76$ Å $c = 4.35$ Å
	α-Fe (bcc)	$a = 2.86$ Å
Lattice mismatch	[0 0 1] α-Fe // [1 $\bar{2}$ 1 0] Fe(C)	$\eta = 0.0\%$
	[$\bar{1}$ 1 0] α-Fe // [1 0 $\bar{1}$ 0] Fe(C)	$\eta = 22.3\%$
	[1 1 0] α-Fe // [0 0 0 1] Fe(C)	$\eta = 0.0\%$
	[0 $\bar{1}$ 1] α-Fe // [1 0 0] Fe_3C	$\eta = 20.61\%$
	[2 1 1] α-Fe // [0 0 1] Fe_3C	$\eta = 3\%$
	[0 1 1] α-Fe // [0 0 0 1] $Fe_{2.4}C$	$\eta = 6.37\%$
	[1 0 1] α-Fe // [1 0 $\bar{1}$ 1] $Fe_{2.4}C$	$\eta = 3.3\%$

4. Conclusions

In this work we have investigated nano-sized precipitates in Ti microalloyed multiphase steel. Two types of Ti(N) precipitates were observed with cubic and faceted morphologies. The faceted precipitates were found in the size range 40–70 nm and the cubic precipitates were found in the size range of 70–120 nm. The cubic precipitates were found with higher nitrogen concentrations and exhibited

slightly larger lattice parameters than the faceted TiN precipitates. Additionally, spherical shaped Ti_2CS precipitates were found with sizes ranging from 20 to 100 nm. Both the cubic and faceted Ti(N) precipitates and Ti_2CS precipitates were found in random orientations with the neighbouring ferrite matrix. A novel iron carbide precipitate was observed in all ferrite grains. The Fe(C) precipitates have sizes ranging from 2 to 5 nm and exhibited disc shaped morphologies. All the Fe(C) precipitates showed a well-defined Pitsch–Schrader (P–S) orientation relationship with the neighbouring ferrite matrix. From the precipitate size, inter-particle spacing and lattice misfit calculations the newly observed Fe(C) precipitates are seen to possess significant potential in enhancing the strength of these steels.

Acknowledgements

This research was carried out under Project Number MC5.06280a in the framework of the Research Program of the Materials innovation institute M2i (www.m2i.nl). The authors would like to thank V. Svechnikov for the TEM sample preparation and E. Peekstok for his help with light microscopic examination, M. Neklyudova for HRTEM analysis and Dr. D.N. Hanlon (Tata Steel RDT) for providing the material for this study and for fruitful discussions.

Appendix A. Supplementary material

Supplementary data associated with this article can be found, in the online version, at http://dx.doi.org/10.1016/j.actamat.2012.09.025.

References

[1] Bhadeshia HKDH. ISIJ Int 2002;42(9):1059–60.
[2] Tirumalasetty GK, van Huis MA, Kwakernaak C, Sietsma J, Sloof WG, Zandbergen HW. Acta Mater 2012;60:1311–21.
[3] Sakuma Y. In: Proc int conf advanced high strength sheet steels for automotive applications. CO: Association for, Iron & Steel Technology; 2004. p. 11–18.
[4] Honeycombe RWK. Met Mater Trans A 1976;7A:915.
[5] Soto R, Saikaly W, Bano X, Issartel C, Rigaut G, Chara A. Acta Mater 1999;47(12):3475–81.
[6] Tirumalasetty GK, van Huis MA, Fang CM, Xu Q, Tichelaar FD, Hanlon DN, et al. Acta Mater 2011;597:406–7415.
[7] Dunlop GL, Carlsson CJ, Frimodig G. Met Trans A 1978;9(2):261–6.
[8] Craven AJ, He K, Garvie LAJ, Baker TN. Acta Mater 2000;48:3857–68.
[9] De AK, Speer JG, Matlock DK. Adv Mater Proc 2003;161:27–30.
[10] Aigner K, Lengauer W, Rafaja D, Ettmayer P. J Alloys Compd 1994;215:121.
[11] Kim W, Park JS, Suh CY, Cho SW, Lee S, Sohn IJ. Mater Trans 2009;50:2897–9.
[12] Saikaly W, Bano X, Issartel C, Rigaut G, Charrin L, Charai A. Met Mater Trans A 2001;32(8):1939–48.
[13] Kulkarni SR, Selva Vennila R, Phatak NA, Sexena SK, Zha CS, Raghy TEl, et al. J Alloys Compd 2008;448:L1.
[14] Fasiska EJ, Jeffrey GA. Acta Cryst 1965;19:463–71.
[15] Hirotsu Y, Nagakura S. Acta Metall 1972;20:645–55.
[16] Lv ZQ, Sun SH, Jiang P, Wang BZ, Fu WT. Comput Mater Sci 2008;42:692–7.
[17] Herbstein EH, Snyman JA. Inorg Chem 1964;3:894–6.
[18] Fang CM, van Huis MA, Zandbergen HW. Phys Rev B 2009;90:224108.
[19] Retief JJ. Powd Diff 1999;14:130–2.
[20] du Plessis HE, de Villiers JPR, Kruger GJ, Steuwer A, Brunelli M. J Synchr Rad 2011;18:266–71.
[21] Fang CM, van Huis MA, Sluiter MHF, Zandbergen HW. Acta Mater 2010;58:2968–77.
[22] Nagakura S, Toyoshima M. Trans Jpn Inst Met 1979;20:100–10.
[23] Jack KH. J Iron Steel Inst 1951;170:248–55.
[24] Roberts CS, Averback BL, Cohen M. Trans Am Soc Met 1953;45:576.
[25] Dijkstra LJ. J Metals 1949;1:252.
[26] Wert CA. J Appl Phys 1949;20:943.
[27] Tsou A, Nutting J, Menter JW. J Iron Steel Inst 1952;172:163.
[28] Boswell FWC. Acta Cryst Camb 1958;11:51.
[29] Leslie WC, Fisher RM, Sen N. Acta Metall 1959;7(9):632–44.
[30] Dieter GE. Mechanical metallurgy. 3rd ed. New York: McGraw-Hill; 1988.
[31] Taran YuN, Novik VI. Met Sci Heat Treat 1971;13(10):818–20.
[32] Gladman T. The physical metallurgy of microalloyed steels. London: The Institute of Materials; 1997.
[33] Gladman T, Holmes B, McIvor ID. Effect of second phase particles on the mechanical properties of steels. London: Iron and Steel Institute; 1971. p. 68.
[34] Sobral MDC, Mei PR, Kestenbach HJ. J Nanosci Nanotechnol 2010;10(2):1235–40.
[35] Bagaryatski YA. Dokl Akad Nauk SSSR 1950;73:1161.